Tropical Cyclone Wind Direction Retrieval From Dual-Polarized SAR Imagery Using Histogram of Oriented Gradients and Hann Window Function

Weicheng Ni, *Student Member, IEEE*, Ad Stoffelen, *Fellow, IEEE*, and Kaijun Ren, *Member, IEEE*

***Abstract*—Accurate knowledge of wind directions plays a critical role in ocean surface wind retrieval and tropical cyclone (TC) research. Under TC conditions, apparent wind streaks induced by marine atmospheric boundary layer rolls can be detected in VV- and VH-polarized synthetic aperture radar (SAR) images. It suggests that though relatively noisy, VH signals may help enhance wind streak orientation magnitudes contained in VV signals and thus to achieve a more accurate wind direction estimation. The study proposes a new method for wind direction retrieval from TC SAR images. Unlike conventional approaches, which calculate wind directions from single-polarization imagery, the method combines VV and VH signals to obtain continuous wind direction maps across moderate and extreme wind speed regimes. The technique is developed based on the histogram of oriented gradient descriptor and Hann window function, accounting for the contribution of neighboring wind streak information (weighted by separation distances). As a case study, the wind directions over four TCs (Karl, Maria, Douglas, and Larry) are derived and verified by estimates from simultaneous dropsonde, ASCAT and ECMWF winds, showing a promising consistency. Furthermore, a more comprehensive statistical analysis is carried out with 14 SAR images, revealing that obtained wind directions have a correlation coefficient of 0.98, a bias of −6.07° and a RMSD of 20.24°, superior to estimates from VV (0.97, −7.84°, and 24.23°, resp.) and VH signals (0.96, −10.46°, and 29.53°, resp.). The encouraging results prove the feasibility of the technique in SAR wind direction retrieval.**

***Index Terms*—Dual-polarized SAR images, Hann window function, histogram of oriented gradient descriptor, tropical cyclone (TC), wind direction.**

I. Introduction

ACCURATE knowledge of tropical cyclone (TC) characteristics plays a central role in TC risk assessments and thus contributes to disaster preparedness and response [1]. It requires a variety of TC metrics, among which the most fundamental ones are TC intensities (which depend on observed maximum sustained wind speeds) and wind direction maps. A series of geophysical model functions (GMFs) have been developed during the last decades to correlate wind speeds, wind direction, and observation geometry to ocean surface roughness measurements [normalized radar cross section, (NRCS)]. Its codependency on speed and direction indicates that the accuracy of wind speed estimation is closely linked to the reliability of wind directions [2] and hence a more reliable and robust wind direction retrieval technique will, in turn, lead to improvements in TC intensity analysis and subsequent risk assessment.

Synthetic aperture radars (SARs) have been widely used for TC measurements [3], [4]. They have the unique capability of cloud penetration and can probe large ocean surface areas at a very high spatial resolution. In particular, they can detect the kilometer-scale wind streaks induced by marine atmospheric boundary layer (MABL) rolls, which are approximately aligned with the mean wind direction [5], [6], [7]. In addition to getting wind directions directly from external wind sources [8], traditional approaches generally calculate wind directions from copolarized (VV/HH) NRCS imagery, because of the high signal sensitivity to wind directions. These methods include the fourier transformation (FFT) method [9], [10], local gradient (LG) method [11], [12], [13], wavelet analysis (WA) method [14], [15], gray-level co-occurrence Matrix (GLCM)-based method [16], and detecting directions of the largest variance [17]. A previous study reports that conventional approaches have an average root-mean-square difference (RMSD) value of around 29° [18].

Wind streaks can be unclear at extreme wind speeds due to the signal saturation phenomenon occurring at VV polarization, which complicates wind direction retrieval. The concerns on the VV signal saturation issue refer back to the research by [19] and subsequently verified by a series of publications [20], [21], [22]. By contrast, the cross-polarized (VH) signals increase monotonically with ocean surface wind speed, with minor apparent NRCS loss of sensitivity up to wind speeds of 75 m/s [23]. The study by Fan et al. [24] suggests improvement in wind direction retrieval using VH signals at extreme winds. They apply the classical LG method to dual-polarized (VV and VH) SAR images, achieving higher accuracy than estimates from

Manuscript received 25 October 2022; revised 7 December 2022; accepted 15 December 2022. Date of publication 19 December 2022; date of current version 5 January 2023. This work was supported in part by the National Natural Science Foundation of China under Grant 42275170 and in part by the science and technology innovation program of Hunan Province under Grant 2022RC3070. The work of Ad Stoffelen is supported by the EUMETSAT OSI SAF and ESA MAXSS projects. *(Corresponding author: Kaijun Ren.)*

Weicheng Ni is with the College of Meteorology and Oceanography and College of Computer Science and Technology, National University of Defense Technology, Changsha 410073, China (e-mail: niweicheng19@gmail.com).

Ad Stoffelen is with the Department of Satellite Observations, Royal Netherlands Meteorological Institute, 3731GA De Bilt, Netherlands (e-mail: ad.stoffelen@knmi.nl).

Kaijun Ren is with the College of Meteorology and Oceanography, National University of Defense Technology, Changsha 410073, China (e-mail: renkaijun@nudt.edu.cn).

Digital Object Identifier 10.1109/JSTARS.2022.3230441

single-polarized signals. Yet, the retrieval process is intrinsically conducted with single-polarizations: wind directions for peripheral TC regions are retrieved using VV-polarizations, whereas estimates inside the eyewall from VH signals. The TC eyewall is determined based on the radius of maximum wind speed (RMW). However, TCs sometimes exhibit asymmetry and lack clear vortex structures, making TC eyewall determination by a constant value quite tricky. Ergo, the method's accuracy is somewhat subject to errors in eyewall determination. Besides, it is worth noting that some studies [25], [26] have attempted to calculate wind directions and wind speeds simultaneously from SAR images. The most representative one is the study by Mouche et al. [26], which combines SAR NRCS measurements and ECMWF information for ocean wind vector estimation. The method adopts VV- and VH-polarized signals together and possesses a promising performance in wind speed estimation. However, the obtained wind directions are largely smoothed and TC centers presented in wind direction maps may not match the real ones because of the overfitting of ECMWF wind directions. As such, a more observation-based wind direction retrieval method for SAR images is attempted here.

We further note that wind streaks are not always observable in SAR images. The study conducted by Levy and Brown reports that MABL rolls are present in 44% and absent in 34% of 1882 SAR images, while for the remainder the decision is not clear [27]. These numbers are close to the later findings by Zhao et al. [28]. Meanwhile, the probability of wind streaks exhibits significant spatial variations, where some regions appear more likely to generate wind streaks [28], [29]. Furthermore, the streaks induced only by winds are practically difficult to distinguish from the streaks caused by other marine phenomena, such as internal waves, surface currents, and atmospheric fronts (moist convection downbursts) [30], [31]. These marine phenomena, as well as the usual heavy precipitation and eyewall replacement cycles (ERCs) occurring during the TC life cycle, can result in abnormal variations of NRCS values within TC SAR images and thus affect the accuracy of conventional approaches. It implies that the wind direction retrieval over a constant small region may generate outliers and thus the incorporation of neighboring information appears beneficial.

This article aims to design a new method combining VV- and VH-polarized signals to achieve reliable wind direction retrieval from TC SAR images. The technique is supposed to generate continuous wind direction estimates throughout TC impact regions and can depict TC vortex structures well. In service of this goal, this study proposes an automatic approach for TC wind direction retrieval using dual-polarizations. The algorithm is developed based on the Histogram of Oriented Gradient (HOG) descriptor [32] and the Hann window function, accounting for the contribution of neighboring wind streak information. The obtained wind directions are comparable to wind products provided by simultaneous dropsonde, Advanced scatterometer (ASCAT) and European Centre for Medium-Range Weather (ECMWF) forecasts. The promising experimental results exhibit the excellent performance of the technique and can contribute to our long-term goal of further exploiting SAR data in meteorological services.

TABLE I
INFORMATION OF TC SAR IMAGES AND AVAILABLE WIND REFERENCE DATA FOR WIND DIRECTION RETRIEVAL AND VALIDATION

TC Name	Satellite	Acquisition Time	Cyclone Location	Wind Reference
Blas	RS-2	2016-07-08 02:45	EPA	ASCAT-A, ECMWF
Karl	S1-A	2016-09-23 22:21	ATL	dropsonde, ASCAT-B ECMWF
Irma	S1-A	2017-09-07 10:29	ATL	dropsonde, ECMWF
Jose	S1-A	2017-09-08 22:02	ATL	dropsonde, ECMWF
Maria	S1-A	2017-09-21 22:44	ATL	dropsonde, ASCAT-A ECMWF
Trami	S1-A	2018-09-28 09:35	WPA	ASCAT-A, ECMWF
Rosa	S1-B	2018-09-30 01:53	EPA	ASCAT-A, ECMWF
Luban	S1-B	2018-10-11 14:20	IND	ASCAT-A, ECMWF
Juliette	S1-A	2019-09-04 13:39	EPA	ASCAT-A, ECMWF
Douglas	S1-A	2020-07-25 03:47	EPA	dropsonde, ASCAT-B ECMWF
Bavi	RS-2	2020-08-25 21:35	WPA	ASCAT-B, ECMWF
Marian	RS-2	2021-03-02 23:19	IND	ASCAT-A, ECMWF
Larry	RS-2	2021-09-07 09:27	ATL	ASCAT-B, ECMWF
Larry	S1-B	2021-09-07 21:46	ATL	dropsonde, ASCAT-B ECMWF

Cyclone locations include eastern pacific (EPA), Western Pacific (WPA), Atlantic (ATL), and Indian Ocean (IND).

This article is organized as follows: A brief description of the datasets used in the study is presented in Section II. Section III elaborates on the technique of wind direction retrieval from dual-polarized SAR images. In Section IV, we present estimation and validation results on SAR TC cases. Finally, Section V concludes this article.

II. DATASET

In the study, 14 Sentinel-1 (S1) SAR and RadarSat-2 (RS-2) SAR images of TCs worldwide ranging from 2016 to 2021 were collected and collocated to simultaneous dropsonde and ASCAT wind measurements. Table I summarizes the information of SAR images and corresponding available wind references. In addition to the actual wind observations, the ECMWF forecasts closest to SAR acquisition times were also used to evaluate wind direction retrievals.

A. RadarSat-2 and Sentinel-1 SAR Images

RS-2 is one of the world's most advanced commercially available Earth observation radar image providers [33] and also the first satellites featuring a cross-polarized mode. The typical

cross-polarized mode operates in an alternating fashion and hence RS-2 is capable of providing C-band ($\sim$5.4 GHz) VV- and VH-polarized ocean surface measurements, in which the latter has a higher sensitivity to extreme winds. RS-2 was launched in December 2007 and has been widely used in TC research [34], [35], [36], [37]. The S1 mission constitutes several satellites (S1-A and -1B, -1 C, and -1D) [38], which possess VV- and VH-polarization SAR capabilities and provide dual-polarized ocean surface acquisitions free of charge [39]. Since 2016, the European Space Agency (ESA) has set up specific SAR acquisition campaigns (Satellite Hurricane Observations Campaign, SHOC) [40] to maximize SAR acquisitions over TCs for both RS-2 and S1 missions to feed research activities. It means SAR passes at extremes have become more common and thus an accurate estimation of TC metrics (including wind direction as addressed in this study) is of high significance in imporved exploitation of SAR images in TC (thermo-)dynamical studies. The TC SAR images used in this article are obtained through SHOC, which has resampled SAR images into 1-km pixel spacing.

B. Dropsonde Wind

GPS dropsonde winds were selected as the reference wind source and collocated with SAR images. It is one of the most popular wind references, directly measuring vertical storm profiles of wind speed, direction, pressure, and other atmospheric variables. A comparison between GPS dropsonde winds and 10-m wind vectors derived from the QuikSCAT satellite near TCs was performed by Chou et al. [41], showing a wind direction RMSE of 17° on the basis of 896 matching samples. However, a further analysis was carried out in 2013 [42] between ASCAT and GPS dropsonde wind products, exhibiting an apparent wind speed-dependent relation for wind direction errors. A larger difference in wind direction occurs at lower wind speed ($<$10 m/s) and vice versa. The wind vector has better quality in the medium wind speed regime, with an RMSD of 28.0° for wind direction. The value is almost equal to the statistical results shown in this study (see "dropsonde" row in Table II, with an RMSD of 29.63°). 10-m ocean surface winds from dropsonde wind profiles were calculated using the WL150 algorithm [43] and collocated with SAR-derived wind directions. In total, 103 dropsondes were collected with a maximum time departure of less than 12 h. Note that SAR and dropsonde measurements can not be directly compared since the former return near-instantaneous measurements of ocean surface roughness, while the latter measure the vertical storm profiles at (slightly) different location or time. The TC movement over time displaces the dropsonde locations with respect to SAR images of the eye of the TC. As such, dropsonde measurements need to be shifted according to TC motion vector and time departure. The dropsonde data are publicly available and can be found at: https://www.aoml.noaa.gov/hrd/data_sub/hurr.html

C. ASCAT Wind

ASCAT is one popular scatterometer type used routinely for real-time TC monitoring. In this study, ASCAT-A/B TC observations with maximum acquisition time departures of less than 3 h were collected and then processed by the ASCAT wind data processor (AWDP) [44] on a swath grid of 12.5 km. The ASCAT data in BUFR and NetCDF format can be ordered online from the EUMETSAT Data Centre (https://www.eumetsat.int/eumetsat-data-centre). Note that the processed ASCAT data need to be shifted spatially to match the TC centers in the collocated SAR images. After that, the ASCAT wind ambiguities were removed using the two-dimensional variational ambiguity removal (2DVAR) [45], which adopted ECMWF operational forecasts as the background. Only the forecast step closest to ASCAT acquisition time is used in the study and for a further description of ECMWF forecast winds we refer to Section II-D. The 2DVAR observation and background error variances are left to their default values.

D. ECMWF Forecasts

As a complement to observations of dropsonde and ASCAT sensors, the study adopts short-range forecasts of 10-m stress-equivalent winds [46] generated by the ECMWF model Integrated Forecasting System (IFS) as wind reference. IFS is the combined atmospheric model and data assimilation system (its currently operational version), combining state-of-the-art meteorological and atmospheric composition modelling [47]. It can provide deterministic hourly forecasts of atmospheric variables with global coverage, including the wind directions needed in this study. Similar to the processing on ASCAT images, the ECMWF forecast winds are shifted to match the TC centres in SAR data.

III. Methodology

A. Histogram of Oriented Gradients

HOG is a feature descriptor which counts the number of occurrences of gradient orientation within a detection window. In contrast to the conventional histogram construction method utilized in the LG method, the HOG descriptor casts a weighted vote for an orientation-based histogram channel according to the gradient magnitudes of pixels. It performs well in detecting texture features. Given a TC SAR VV/VH NRCS image (I) of interest [e.g., the SAR VH NRCS image of TC Karl, see Fig. 1(a)], the main steps of HOG computation can be summarized as follows:

1) Cell Division: Divide the SAR image into a series of small adjacent nonoverlapping $c_1 \times c_2$ regions ("*Cells*"), as displayed in Fig. 1(b).

2) Gradient computation: For each pixel with indices (i, j), the spatial gradients in horizontal ($f_x(i, j)$) and vertical direction ($f_y(i, j)$) are computed. After that, the gradient magnitude $m(i, j)$ and orientation $\theta(i, j)$ can be estimated in the form of

$$m(i,j) = \sqrt{(f_x(i,j)^2 + f_y(i,j)^2)} \tag{1a}$$

$$\theta(i,j) = tan^{-1}\frac{f_y(i,j)}{f_x(i,j)}. \tag{1b}$$

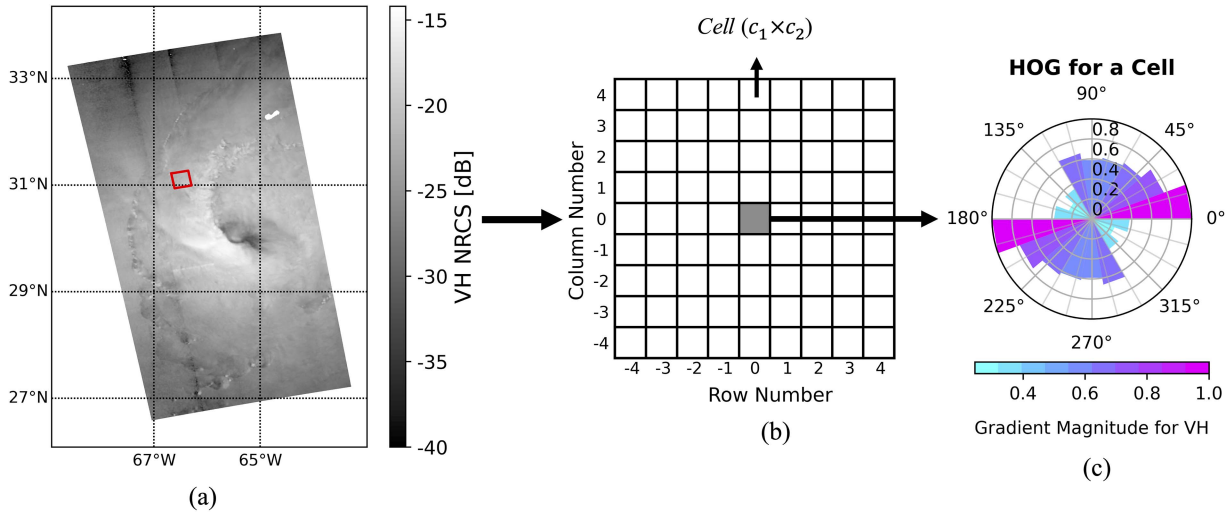

Fig. 1. Procedure of SAR image (a) division into Cells (b) and HOG generation over each Cell (c). The right panel presents obtained HOG (normalized by the maximum gradient magnitude value) from VH signals over the red square area, which shows apparent orientation features. The gradient magnitudes indicate the probabilities of wind directions. Note that the 180° symmetry is imposed during the calculation to display the inherent 180° wind direction ambiguity.

3) Orientation binning: Accumulate the histogram over each *Cell* by counting the gradient magnitude of pixels in the different orientation bins. Note that the counts are interpolated bilinearly between neighboring bins to reduce aliasing [32]. The study sets a direction bin size of 20° and thus has the interval number n of $180/20 = 9$.

Fig. 1(c) presents the obtained histogram of oriented gradients from VH NRCS signals over a single $Cell$ [the red square region in Fig. 1(a)]. Note that the 180° symmetry is imposed during the calculation. For wind ambiguity removal, we refer to Section III-D. The gradient magnitudes are normalized by the maximum gradient magnitude value. As can be observed, VH NRCS signals exhibit apparent orientation features, showing the possible benefit of wind direction retrieval from VH signals. The finding is consistent with the conclusion by [24].

B. Incorporation of Neighboring Information Using Hann Window Function

After that, build *Blocks* consisting of $M \times N$ *Cells* (two adjacent *Blocks* can overlap, e.g., four *Blocks* displayed in left panels in Fig. 2) and then normalize histograms of $Cell_{i,j}$ ($\xi_{i,j}$) of interest over the subordinate *Block* using a L1-norm block normalization method

$$\xi'_{i,j} = \sqrt{\frac{\xi_{i,j}}{|\zeta| + e}} \tag{2}$$

where $\xi'_{i,j}$ indicates the normalized the histogram of $Cell_{i,j}$ and e stands for a small constant. ζ represents the histogram of the *Block*, obtained by integrating all $\xi_{i,j}$ within this *Block:* $\zeta = \{\xi_{1,1}, \xi_{1,2}, \ldots, \xi_{M,N}\}$.

Different from the traditional HOG descriptor, the obtained $\xi'_{i,j}$ is improved and calculated as the average of all *Cell* HOGs contained in the same *Block*, weighted by separation distances to the target $Cell_{i,j}$; see right panels in Fig. 2. The weights

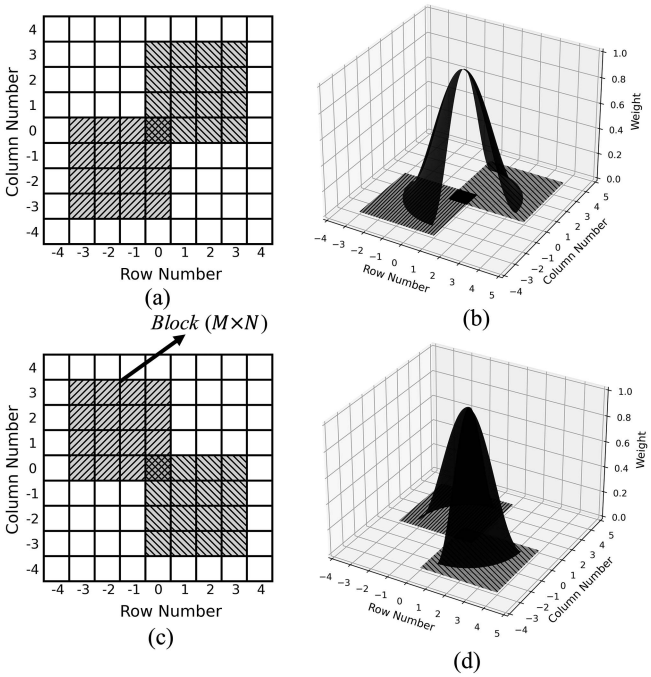

Fig. 2. Block normalization process and the incorporation of neighbouring information using Hann window function. Suppose an interested $Cell$ with indices (0,0), i.e., $Cell_{0,0}$, and $Blocks$ consisting of 4×4 $Cells$. $Cell_{0,0}$ is subordinative to 16 $Blocks$ in total, among which four are shown in the left panels. The HOG of $Cell_{0,0}$ is calculated as the average of all $Cell$ HOGs contained in the same $Block$, weighted by the separation distances. The right panels illustrate variations of weights with regard to separation distances to $Cell_{0,0}$.

are determined using a Hann Window function. The weighted average calculation process can alleviate the impacts of local severe NRCS variations resulting from the precipitation and wave breaking in TCs and thus improve the continuity of wind direction products. Assuming a *Block* consisting of $M \times N$

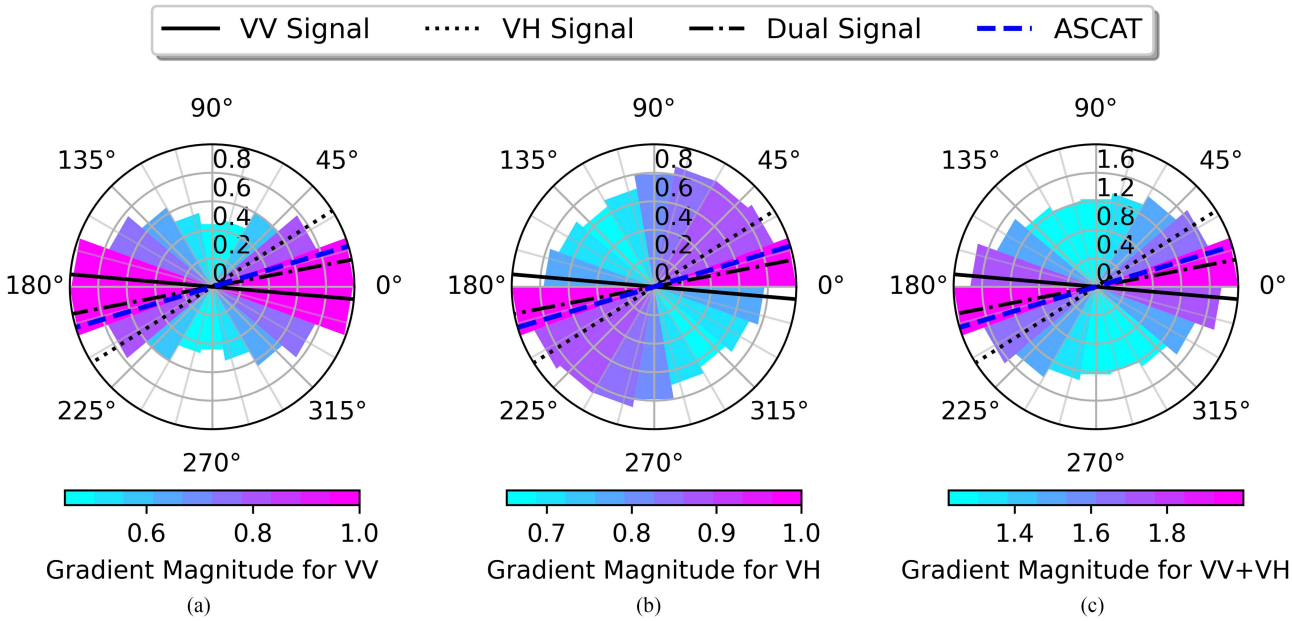

Fig. 3. Obtained HOGs from VV- (a), VH- (b) and dual-polarized (c) SAR signals over the red square area in Fig. 1(a). The solid, dotted and dash-solid lines indicate the wind directions calculated from VV, VH, and VV+VH signals, respectively. The blue dashed lines present the wind direction calculated from collocated ASCAT winds. One can find that the orientation obtained from dual-polarized signals is more in line with the ASCAT estimate. It suggests the possible benefit of combining VV and VH signals for wind direction retrieval.

$Cells$, the HOG of $Cell_{i,j}$ ($\xi''_{i,j}$) of interest is calculated as

$$\xi''_{i,j} = \sum_{p,q=1}^{M,N} w_{p,q}\xi'_{p,q} \tag{3a}$$

$$w_{p,q} = \cos^2\left(\pi\frac{x}{L}\right),\ 0 \le x \le \frac{L}{2} \tag{3b}$$

where i and j denote the subscripts of the interested $Cell_{i,j}$ in the $Block$; L is the length in the Hann window function, defined as $L = \sqrt{M^2+N^2}$; $\xi'_{p,q} = (a_1, a_2, \ldots, a_n)$ indicates the magnitudes in different orientation intervals for arbitrary $Cell_{p,q}$ in the *Block* while n presents the interval number with a value of 9. x means the spatial distance between $Cell_{p,q}$ and target $Cell_{i,j}$, calculated in the form of $x = \sqrt{(i-p)^2+(j-q)^2}$.

Furthermore, the calculation process for $Cell_{i,j}$ will be repeated over all $Blocks$ ($M \times N$ $Blocks$ at most) containing the *Cell*. Labelling obtained HOG from $Cell_{i,j}$ in $Block_t$ as $\xi^{''t}_{i,j}$ and assuming $Cell_{i,j}$ is subordinate to T *Blocks* in total, then the final HOG of $Cell_{i,j}$ can be estimated in the form of

$$\xi'''_{i,j} = \sum_{t=1}^{T} \xi^{''t}_{i,j},\ \ T \le M \times N \tag{4}$$

where t represents the subscript of the *Block*.

The left two panels in Fig. 3(c) exhibit the obtained HOGs over the red square area in Fig. 1(a) from VV ($\overline{\xi'''}_{VV}$) and VH signals ($\overline{\xi'''}_{VH}$), where the gradient magnitudes indicate the probabilities of wind directions. The overbar means normalizing ξ''' by the maximum gradient magnitude. Fig. 3(c) shows the corresponding HOG of $\overline{\xi'''}_{VV} + \overline{\xi'''}_{VH}$.

C. Wind Direction Estimation

The wind directions are obtained by minimizing the cost function

$$J(\theta') = \sum_{i=1}^{n} \left[(|\theta' - \theta^o| \cdot r_{VV}(\theta^o)) + (|\theta' - \theta^o| \cdot r_{VH}(\theta^o))\right] \tag{5}$$

where $r_{VV}(\theta^o)$ and $r_{VH}(\theta^o)$ indicate the magnitudes in different orientation intervals for VV and VH signals; n stands for the interval number; $\theta' - \theta^o$ indicate the radian differences modulo $\pm\pi$ between obtained wind direction (θ') and various orientations (θ^o).

The solid, dotted, and dash-solid lines in Fig. 3 indicate the wind directions determined from VV, VH, and VV+VH signals, individually. For comparison, the wind direction from collocated ASCAT winds is plotted; see blue dashed lines in Fig. 3. It is worth noting that the wind direction offered by ASCAT measurement is closer to the orientation retrieved from dual-polarized signals. Thus, it is reasonable to infer that the combination of VV- and VH-polarized signals perhaps possess a better capability for wind direction estimation, especially in the vicinity of the TC eyewall area where the wind speeds are relatively high. A further statistical assessment will be performed in Section IV.

D. Wind Ambiguity Removal

Wind direction ambiguities are removed taking advantage of the parametric inflow-angle model [48], which can provide prior wind directions within the TC impact area. The storm-relative inflow angle α_{SR} is defined as the arctangent of the ratio of radial (v_r) to tangential (v_t) wind components: $\alpha_{SR} = \arctan(v_r/v_t)$. Thus, one has negative α_{SR} values when $v_r < 0$. Zero values

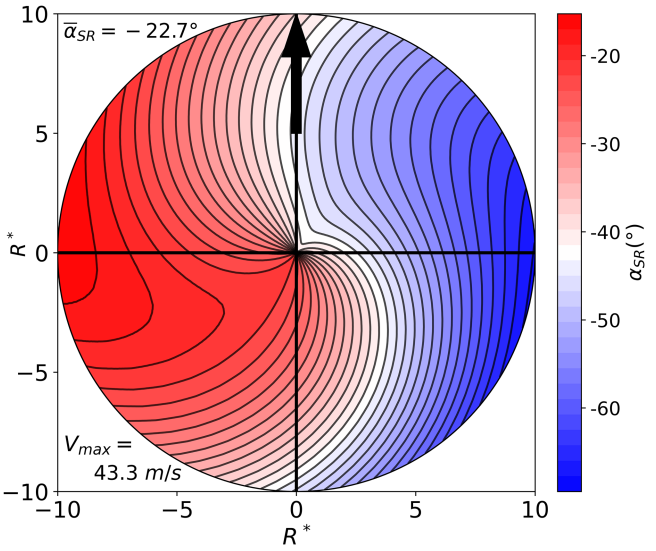

Fig. 4. Storm-relative inflow-angles calculated with the parametric inflow-angle model for TC Karl. The arrow indicates the storm movement direction. Horizontal and vertical axes R^* indicate the normalized radial distances by observed RMW.

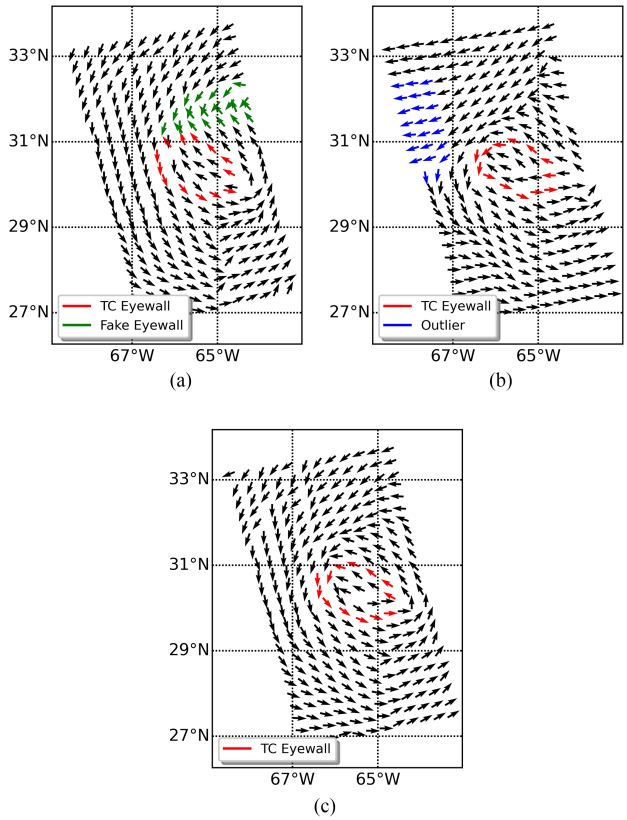

Fig. 5. Wind vector fields of TC Karl estimated from VV- (a), VH- (b) and dual- (c) polarizations. The red arrows present the TC eyewall determined with the GLGCM method. The green and blue arrows indicate outliers of wind direction retrievals from VV and VH signals. It can be found that the wind vector fields retrieved from dual-polarized signals are smooth and more consistent with the visual results.

of α_{SR} suggest that the wind vectors are tangential to the radial directions. In the study, the wind direction ambiguity removal procedure consists of five steps: 1) determine the TC centre positions using the gray level-gradient co-occurrence matrix (GLGCM)-based method [49]; 2) calculate the TC motion speed V_s at the image acquisition time according to TC locations recorded by best-track data at different time points. The latest version 4 of the International Best Track Archive for Climate Stewardship (IBTrACS) dataset [50], [51] is used in the study. 3) estimate TC intensity using the method proposed by [52]; 4) derive prior wind directions following the parametric inflow-angle model; 5) select wind direction solutions closest to estimates provided by the inflow-angle model.

Fig. 4 displays the inflow-angle map for TC Karl (acquired on September 23, 2016) with V_s of 7.0 m/s and TC intensity of 43.3 m/s. It has a mean inflow-angle value $\overline{\alpha}_{SR}$ of $-22.7°$. Note that the value of parameter b in (2) in [48] should be -0.09 but not -0.9.

IV. Results and Discussions

Fig. 5 presents the wind direction images calculated from VV-, VH-, and dual-polarized SAR images of TC Karl using the proposed method. The optimum $Cell$ and $Block$ sizes are determined by minimizing RMSDs between retrieved wind directions and estimates provided by the parametric inflow-angle model over the TC eyewall region.

The red wind vectors in Fig. 5 stand for the TC eyewall determined by the GLGCM method. As one may note, it is difficult to capture the TC eyewall with merely VV signals because of the signal saturation phenomenon at extremes and the NRCS co-dependency on speed and direction [see Fig. 5(a)]. Under this condition, the wind streak orientations can be unclear and thus result in the smearing of the TC eyewall structure. In practice, sharp wind direction variations can be detected in the vicinity of the TC eyewall, which resembles an extension of eyewall (noted as "fake eyewall" in this study), see green wind vectors in Fig. 5(a). On the other hand, VH-retrieved wind vectors, though depicting the TC eyewall well, contain a clear divergence in the northwest; see blue wind vectors shown in Fig. 5(b). It is supposed to result from calibration artefacts (bands in TC NRCS images) and the low sensitivity of VH signals to wind direction. Besides, VH has a lower signal-to-noise ratio (SNR) in low wind speed areas than VV, which may hamper the detection of streaks. By contrast, the wind directions acquired from dual-polarized signals [see Fig. 5(c)] are more continuous and demonstrate a better agreement with visual results.

Moreover, the dual-signal retrieved wind directions are compared with wind reference estimates from collocated dropsonde, ASCAT wind measurements and ECMWF forecasts, as Fig. 6(a)–(c) illustrate. The black arrows indicate wind vectors calculated from dual-polarized SAR images, while red arrows those from auxiliary wind sources. A satisfactory agreement can be observed between SAR retrievals and wind reference estimates. Apart from the visual comparisons, Fig. 6(d) shows a scatter plot of calculated wind directions versus estimates from the three wind references, having a correlation coefficient (CC) of 0.98, a bias of $-3.52°$ and a RMSD of 20.74°. The

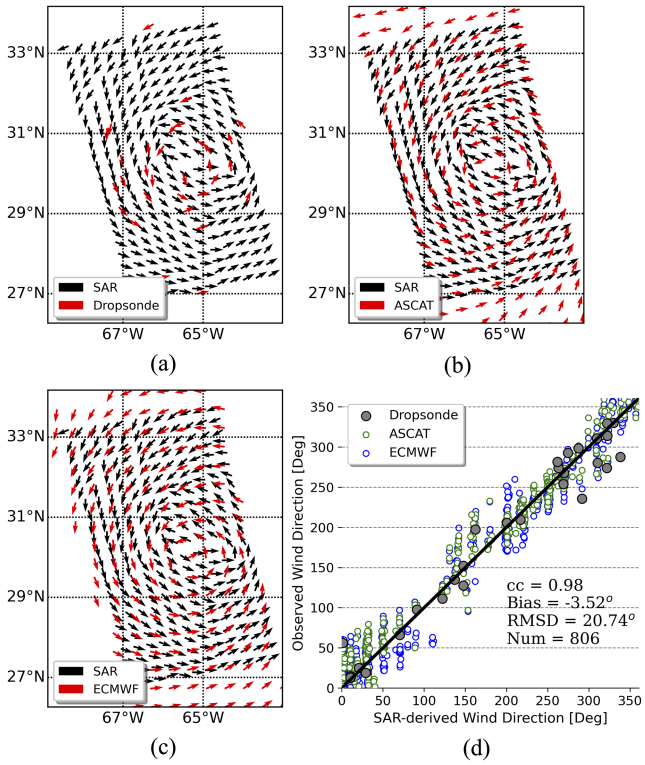

Fig. 6. SAR-retrieved wind vectors (from dual-polarized signals) of TC Karl versus estimates provided by dropsonde (a), ASCAT wind measurements (b) and ECMWF forecasts (c). (d) Scatter plot of SAR-retrieved wind directions versus collocated estimates from the three wind references.

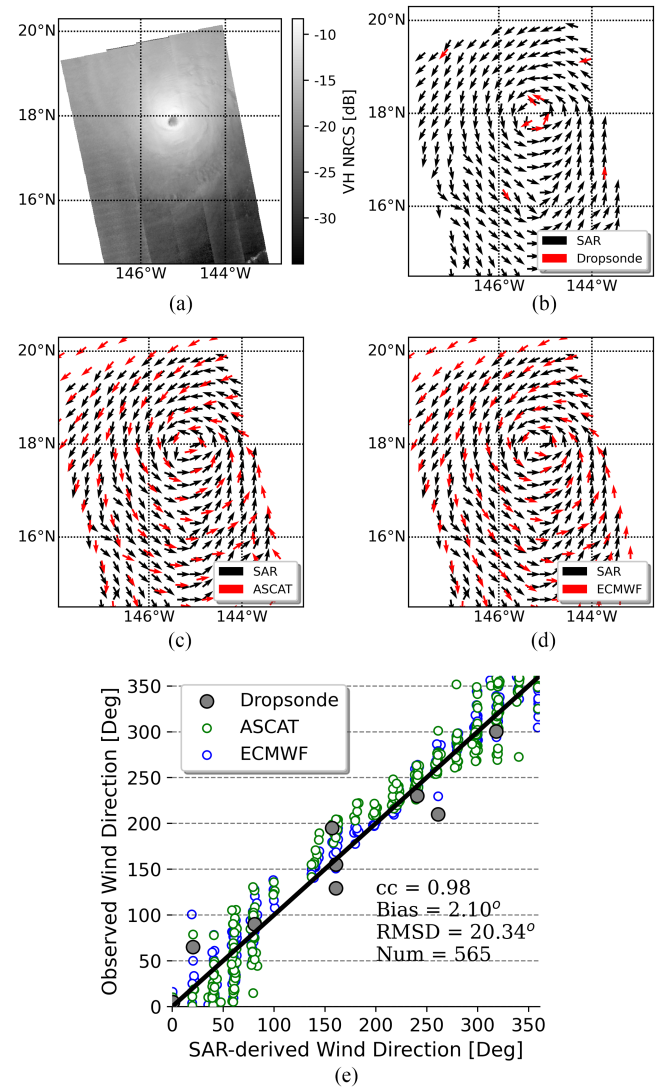

Fig. 7. (a) TC Douglas (acquired on July 25, 2020) imaged by SAR VH signals. Obtained wind vectors from dual-polarized signals (the black arrows) versus estimates from collocated dropsonde (b), ASCAT wind measurements (c), and ECMWF forecasts (d). (e) Scatter plot of SAR-retrieved wind directions versus collocated estimates from the three wind references.

technique is further employed for more TC cases, wherein the dropsonde, ASCAT and ECMWF wind estimates are all available. Fig. 7 presents the retrieved ocean surface wind vectors from dual-polarized SAR images of TC Douglas (acquired on July 25, 2020), wherein the lower panel shows the scatter plot of SAR-retrieved wind directions versus estimates from the collocated wind references. The CC is 0.98, the bias $-2.10°$, and the RMSD 20.34°. Fig. 8 presents the corresponding results for TC Larry (acquired on September 7, 2021), with a CC of 0.98, a bias of $-5.61°$ and an RMSD of 19.16°. The satisfying agreement between SAR-derived wind directions and wind reference estimates proves the feasibility and robustness of the technique.

However, in practice, more factors may need to be taken into account when attempting to retrieve wind directions in near-shore regions. Fig. 9 shows the wind vectors obtained from dual-polarized SAR images of TC Maria (acquired on September 21, 2017) versus estimates from the wind references. The statistical analysis result is shown in Fig. 9(e), where the CC is 0.95, the bias $-21.05°$ and the RMSD 32.76°. The relatively poorer quality is expected to originate from the relatively large acquisition time difference between SAR and ASCAT data and the impacts of TC landfall on near shore wind streaks. Note that TC Maria was still hovering over the ocean when imaged by ASCAT. However, when it was captured by SAR data, the southern part of TC Maria was over land. It is reasonable to assume that wind-induced streaks shown in the southern regions can be influenced by coastal effects, which will inevitably disturb the wind direction retrieval process. As indicated by Li et al. [53], [54], the shallow water forcing can significantly affect the coastal sea surface manifestation shown in the SAR images and thus result in the disagreement between wind directions (from auxiliary wind references) and streak orientations. On the other hand, a high agreement between wind direction estimates and the references can be observed for other regions, e.g., the northern and eastern parts of TC Maria. However, when moving from the open ocean to coastal regions, e.g., the southern part of the SAR images, the retrieved wind directions tend to be from west to east (zonal), while wind references provided by ASCAT and ECMWF blow meridionally; see the coastal regions wrapped by the orange squares in Fig. 9(c) and (d). As a result, it leads to some ill-collocated pairs between SAR and ASCAT/ECMWF, i.e., the points wrapped by the orange square in Fig. 9(d). The bias and RMSD values would be highly improved when

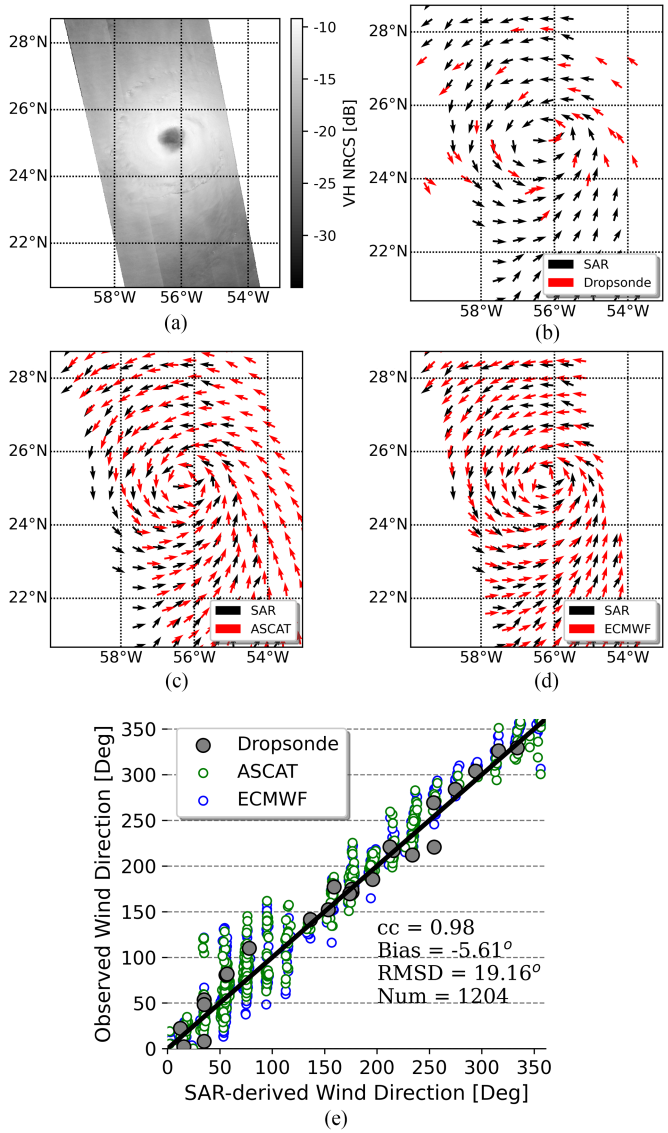

Fig. 8. (a) TC Larry (acquired on September 7, 2021) imaged by SAR VH signals. Obtained wind vectors from dual-polarized signals (the black arrows) versus estimates from collocated dropsonde (b), ASCAT wind measurements (c), and ECMWF forecasts (d). (e) Scatter plot of SAR-retrieved wind directions versus collocated estimates from the three wind references.

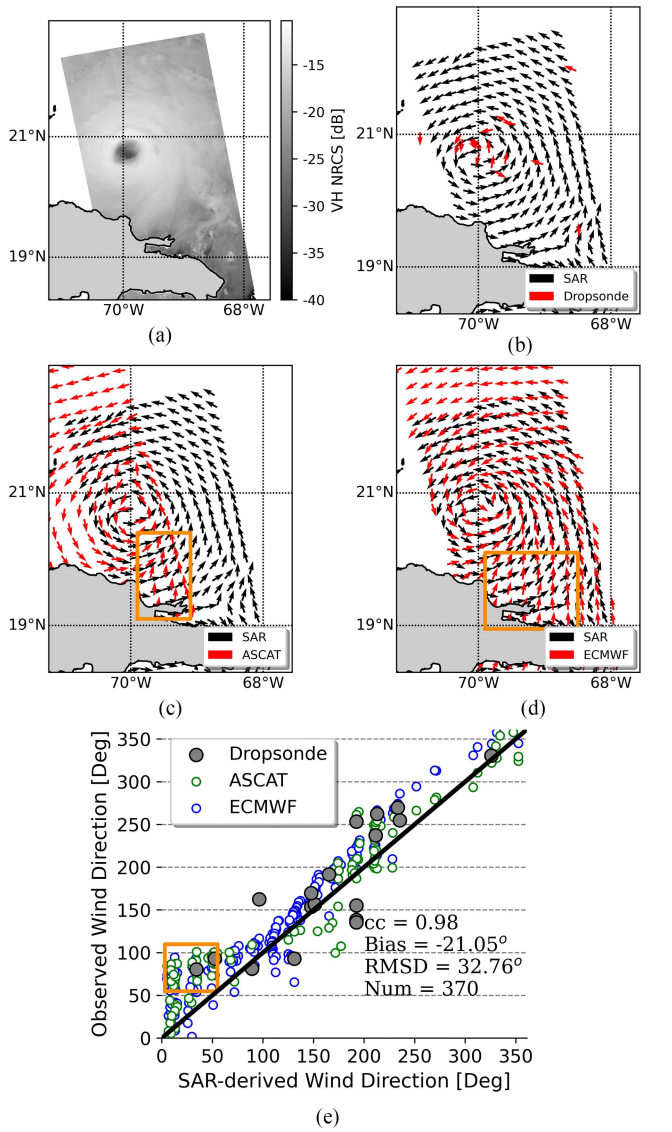

Fig. 9. (a) TC Maria (acquired on September 21, 2017) imaged by SAR VH signals. The obtained wind vectors from dual-polarized signals (the black arrows) versus estimates from collocated dropsonde (b), ASCAT wind measurements (c), and ECMWF forecasts (d). A high agreement between wind direction estimates and the references can be observed for the northern and eastern parts of TC Maria. However, when moving from the open ocean to coastal regions, e.g., the coastal regions wrapped by the orange squares in (c) and (d), the retrieved wind directions tend to be from west to east (zonal), while wind references provided by ASCAT and ECMWF blow meridionally. The discrepancy reflects the impacts of TC landfall on near shore wind direction retrieval. (e) Scatter plot of SAR-retrieved wind directions versus collocated estimates from the three wind references. The points wrapped by the orange square present the ill-collocated pairs between SAR and ASCAT/ECMWF due to coastal effects.

discarding these pairs. Nevertheless, it is noteworthy that the proposed method can guarantee the continuity of wind vectors from coastal (which is considered noisier) to offshore regions. To improve the retrieval accuracy for the near shore regions, some additional factors besides ocean bottom friction effects need to be accounted for, such as the effects of biological/oil slicks and ocean currents. Yet, these are beyond the scope of the paper and are planned to be solved in future work.

Apart from the case-by-case tests, the validation of the proposed technique is extended to more TC SAR images. Table I lists the SAR images used in the study and corresponding available wind references. Note that ECMWF forecasts can always act as the wind reference due to their global coverage. A statistical comparison is performed between SAR-retrieved wind directions and wind reference estimates, as shown in Fig. 10 . There are 11 246 points in total. For further comparison, the left and middle panels in Fig. 10 show the scatter plots of wind direction retrieved from VV and VH polarizations, respectively, while Fig. 10(c) shows the estimated results from dual-polarized SAR images. It is worth noting that VH-polarized signals, though qualified for wind direction estimation, have higher bias and RMSD values (-10.46° and 29.53°, respectively) as compared to VV-retrieved results (with bias and RMSD values of -7.84° and 24.23°, respectively). The relatively poorer

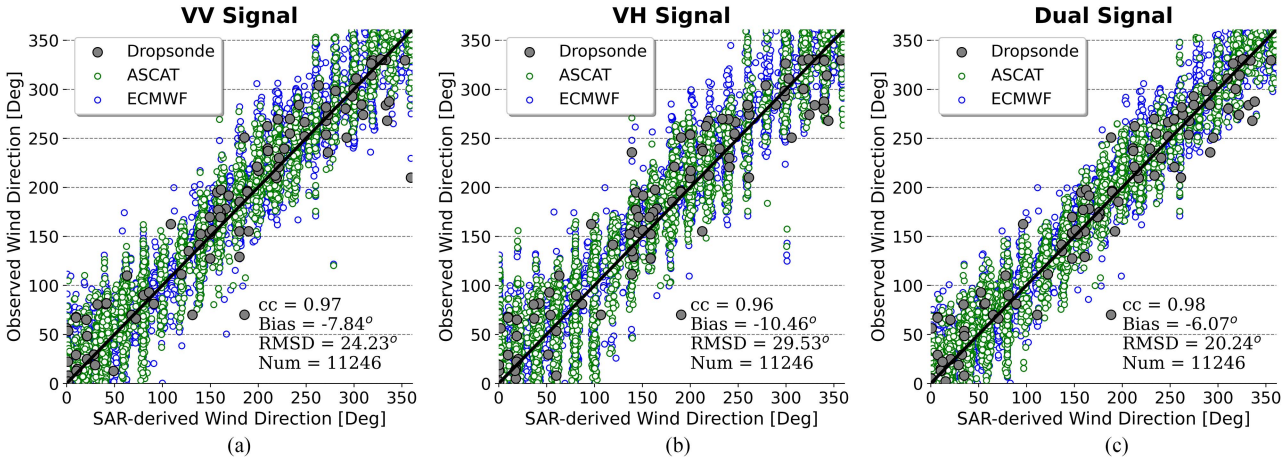

Fig. 10. Scatter plots of SAR-retrieved wind directions from VV- (a), VH- (b) and dual-polarized (c) signals versus estimates from collocated dropsonde, ASCAT and ECMWF wind references. As can be observed, the wind direction estimates from dual-polarized signals using the proposed method have the highest CC value while the lowest bias and RMSD values.

TABLE II
CORRELATION COEFFICIENT, BIAS AND RMSD VALUES OF WIND DIRECTION RETRIEVALS FROM VV-, VH- AND DUAL-POLARIZATIONS WITH RESPECT TO ESTIMATES FROM DIFFERENT WIND REFERENCES

Wind Reference	VV Signal			VH Signal			Dual Signal			Number of Points
	CC	Bias	RMSD	CC	Bias	RMSD	CC	Bias	RMSD	
Dropsonde	0.95	-3.86°	34.48°	0.95	-7.02°	34.50°	0.96	-1.90°	29.63°	103
ASCAT	0.97	-8.16°	24.13°	0.96	-10.70°	30.67°	0.98	-5.95°	20.89°	4,417
ECMWF	0.97	-7.69°	24.10°	0.96	-10.35°	28.68°	0.98	-5.72°	19.62°	6,726
All Dataset	0.97	-7.84°	24.23°	0.96	-10.46°	29.53°	0.98	-6.07°	20.24°	11,246

quality of VH-retrieved results is in line with the statistical results reported by [55]. It may attribute to the lower SNR and insensitivity to wind direction in moderate and low wind speed regimes. Though noisy, VH signals contain considerable texture features and the combination of dual signals can help enhance the gradient magnitudes of true wind streak orientations in HOGs and thus achieve a more accurate wind direction estimation. The estimates from dual-polarized signals using the proposed method reduces the bias and RMSD values by 2.77° (4.39°) and 3.99° (9.29°) compared with VV (VH) signal estimates, i.e., an improvement of 35% (42%) and 16% (31%). Furthermore, the statistical results of VV, VH, and dual signal retrieved results with regard to the individual wind references are presented in Table II. The last row presents the analysis results shown in Fig. 10 for the sake of completeness. When comparing with dropsonde measurements, obtained wind directions have a CC of 0.96, a bias of $-1.90°$ and an RMSD of 29.63°; when validated by ASCAT products, the CC, bias, and RMSD values are 0.98, $-5.95°$, and 20.89°, respectively; when validated by ECMWF forecasts, the CC, bias and RMSD are 0.98, $-5.72°$, and 19.62°, respectively. They all surpass the retrievals from single-polarizations (VV or VH). The encouraging experimental results prove the advantage of dual-polarized signals for wind direction estimation and the reliability of the technique.

Furthermore, Table III gives a summary of SAR wind direction estimation performance using traditional FFT and LG approaches from various published papers. The accuracy of the FFT (LG) algorithm is in the range of $23°\sim 37°$ ($21°\sim 38°$), with an average RMSD value of 28.96° (32.52°). For comparison, the performance of the proposed technique is added to Table III, which is specified as "dual-HOG" method to suggest that it is the implementation of wind direction retrieval from dual-polarization signals using the HOG descriptor. It can be found that the proposed method possesses a higher accuracy compared to the traditional approaches. However, it is noteworthy that the uncertainties of selected wind references, different atmospheric conditions and coastal effects will inevitably impact accuracies of these methods. As such, a more comprehensive comparison between the proposed method and traditional approaches at different sea areas, high/low wind speed regimes and inshore/offshore regions is required for better guidance on TC research. It will be a topic in our future work.

V. CONCLUSION

Wind direction estimation is key for ocean-surface wind field retrieval and TC structure analysis. For most current GMFs, wind directions are requisite input parameters when calculating wind speeds. As a result, the accuracy of TC intensity estimation is largely subject to errors in wind direction. In TC conditions, apparent wind streaks induced by MABL rolls can be detected from both VV and VH polarizations. It suggests that although relatively noisy, VH signals may be used to enhance true wind streak orientation information contained in VV signals and hence achieve a more accurate wind direction estimate.

A new method for TC wind direction retrieval from dual-polarized SAR images is elaborated here, taking advantage of

TABLE III
PERFORMANCE SUMMARY OF FFT AND LG WIND DIRECTION ESTIMATION APPROACHES FROM VARIOUS PUBLICATIONS

Source	Wind Reference	Method	RMSD
Fetter et al. 1998 [56]	Buoy	FFT	37.00°
Horstman et al. 2002 [11]	HIRLAM[a]	LG	21.60°
Wackerman et al. 2003 [17]	Buoy	FFT	34.70°
Carvajal et al. 2013 [57]	Coastal *in situ*	LG	35.20°
	Offshore *in situ*	LG	26.90°
	ASCAT	LG	38.20°
	GFS Model[b]	LG	36.50°
Zhou et al. 2017 [13]	ECMWF	FFT	30.22°
	ECMWF	LG	36.10°
	CCMP[c]	FFT	25.42°
	CCMP	LG	36.65°
Zheng et al. 2018 [16]	ECMWF	FFT	23.00°
	ECMWF	LG	30.96°
	CCMP	FFT	23.43°
	CCMP	LG	30.53°
This study	**dropsonde, ASCAT, ECMWF**	**dual-HOG**	**20.24°**

[a]The Danish High-Resolution Limited-Area Model (HIRLAM).
[b]The Global Forecast System (GFS) Model.
[c]Cross-Calibrated Multi-Platform (CCMP) wind vector product.

the HOG descriptor and Hann window function. The case studies over TC Karl, Maria, Douglas, and Larry indeed illustrate that the combination of VV and VH signals is capable of acquiring more accurate wind direction, while the estimation from single polarizations is hampered by signal phenomenon (e.g., VV signal saturation at extremes) and the lower SNR (e.g., VH signals at moderate winds). In addition, the obtained wind directions are quantitatively validated by observations from collocated dropsondes and ASCAT and by ECMWF forecasts. According to the statistical analysis results, the calculated results from dual-polarized signals using the proposed technique have a CC of 0.98, bias of $-6.17°$ and RMSD of $20.24°$, superior to estimates from VV (0.97, $-7.84°$, and $24.23°$, resp.) and VH signals (0.96, $-10.46°$, and $29.53°$, resp.). Similar statistical analysis results can be observed when comparing to a single wind reference.

The work will extend to more TCs for deeper evaluation in future studies. However, challenges remain, such as the optimal weights of VV and VH signals in HOGs (which are now taken equal) and the issue of calibration stripe noise (which can generate fake gradient orientations in SAR images). Besides, a more specific wind direction retrieval scheme will need to be developed for coastal regions to alleviate the impacts of coastal dynamics. Moreover, considering the multiple wind solutions from VV-, VH-, and dual-polarizations, it is possible to improve the current SAR wind direction fields using the 2DVAR scheme. Such issues will be subject to future research.

ACKNOWLEDGMENT

Most datasets used in this study are provided by the EUMETSAT OSI SAF. The authors would like to thank ESA and Institut Français de Recherche pour l'Exploitation de la Mer (IFREMER) for SAR data obtained through SHOC and support through the MAXSS project. Authors would also like to thank Gerd-Jan van Zadelhoff for help in accessing the SAR data.

REFERENCES

[1] K. M. Wilson, J. W. Baldwin, and R. M. Young, "Estimating tropical cyclone vulnerability: A review of different open-source approaches," *Hurricane Risk Changing Climate*, pp. 255–281, Sep. 2022.
[2] P. W. Vachon and F. W. Dobson, "Wind retrieval from RADARSAT SAR images: Selection of a suitable C-band HH polarization wind retrieval model," *Can. J. Remote Sens.*, vol. 26, no. 4, pp. 306–313, 2000.
[3] K. Friedman and X. Li, "Storm patterns over the ocean with wide swath SAR," *Johns Hopkins Univ. Appl. Phys. Lab Tech. Dig.*, vol. 21, no. 1, pp. 80–85, 2000.
[4] X. Li et al., "Tropical cyclone morphology from spaceborne synthetic aperture radar," *Bull. Amer. Meteorological Soc.*, vol. 94, no. 2, pp. 215–230, 2013.
[5] W. Alpers and B. Brümmer, "Atmospheric boundary layer rolls observed by the synthetic aperture radar aboard the ERS-1 satellite," *J. Geophys. Res., Oceans*, vol. 99, no. C6, pp. 12613–12621, 1994.
[6] R. C. Foster, "Why rolls are prevalent in the hurricane boundary layer," *J. Atmospheric Sci.*, vol. 62, no. 8, pp. 2647–2661, 2005.
[7] L. Huang et al., "Tropical cyclone boundary layer rolls in synthetic aperture radar imagery," *J. Geophys. Res., Oceans*, vol. 123, no. 4, pp. 2981–2996, 2018.
[8] B. Duan, W. Zhang, X. Yang, H. Dai, and Y. Yu, "Assimilation of typhoon wind field retrieved from scatterometer and SAR based on the huber norm quality control," *Remote Sens.*, vol. 9, no. 10, 2017, Art. no. 987.
[9] T. Gerling, "Structure of the surface wind field from the seasat SAR," *J. Geophys. Res.: Ocean.*, vol. 91, no. C2, pp. 2308–2320, 1986.
[10] S. Lehner, J. Horstmann, W. Koch, and W. Rosenthal, "Mesoscale wind measurements using recalibrated ERS SAR images," *J. Geophys. Res., Ocean.*, vol. 103, no. C4, pp. 7847–7856, 1998.
[11] J. Horstmann, W. Koch, S. Lehner, and R. Tonboe, "Ocean winds from RADARSAT-1 ScanSAR," *Can. J. Remote Sens.*, vol. 28, no. 3, pp. 524–533, 2002.
[12] W. Koch, "Directional analysis of SAR images aiming at wind direction," *IEEE Trans. Geosci. Remote Sens.*, vol. 42, no. 4, pp. 702–710, Apr. 2004.
[13] L. Zhou et al., "An improved local gradient method for sea surface wind direction retrieval from SAR imagery," *Remote Sens.*, vol. 9, no. 7, 2017, Art. no. 671.
[14] Y. Du, P. W. Vachon, and J. Wolfe, "Wind direction estimation from SAR images of the ocean using wavelet analysis," *Can. J. Remote Sens.*, vol. 28, no. 3, pp. 498–509, 2002.
[15] X. Zhou et al., "Estimation of tropical cyclone parameters and wind fields from SAR images," *Sci. China Earth Sci.*, vol. 56, no. 11, pp. 1977–1987, 2013.
[16] G. Zheng et al., "Development of a gray-level co-occurrence matrix-based texture orientation estimation method and its application in sea surface wind direction retrieval from SAR imagery," *IEEE Trans. Geosci. Remote Sens.*, vol. 56, no. 9, pp. 5244–5260, Sep. 2018.
[17] C. Wackerman, J. Horstmann, and W. Koch, "Operational estimation of coastal wind vectors from RADARSAT SAR imagery," in *Proc. IEEE Int. Geosci. Remote Sens. Symp.*, 2003, vol. 2, pp. 1270–1272.
[18] C. Wackerman, W. Pichel, and P. Clemente-Colon, "Automated estimation of wind vectors from SAR," in *Proc. 12th Conf. Interact. Sea Atmos.*, 2003, pp. 1–8.
[19] M. A. Donelan and W. J. Pierson Jr, "Radar scattering and equilibrium ranges in wind-generated waves with application to scatterometry," *J. Geophys. Res., Ocean.*, vol. 92, no. C5, pp. 4971–5029, 1987.
[20] W. J. Donnelly et al., "Revised ocean backscatter models at C and ku band under high-wind conditions," *J. Geophys. Res., Oceans*, vol. 104, no. C5, pp. 11485–11497, 1999.
[21] D. E. Fernandez, J. Carswell, S. Frasier, P. Chang, P. Black, and F. Marks, "Dual-polarized C- and Ku-band ocean backscatter response to hurricane-force winds," *J. Geophys. Res., Oceans*, vol. 111, no. C8, pp. 1–17, 2006.
[22] H. Fang, T. Xie, W. Perrie, G. Zhang, J. Yang, and Y. He, "Comparison of C-band quad-polarization synthetic aperture radar wind retrieval models," *Remote Sens.*, vol. 10, no. 9, 2018, Art. no. 1448.
[23] A. Mouche, B. Chapron, J. Knaff, Y. Zhao, B. Zhang, and C. Combot, "Copolarized and cross-polarized SAR measurements for high-resolution description of major hurricane wind structures: Application to irma category 5 hurricane," *J. Geophys. Res., Oceans*, vol. 124, no. 6, pp. 3905–3922, 2019.

[24] S. Fan, B. Zhang, A. A. Mouche, W. Perrie, J. A. Zhang, and G. Zhang, "Estimation of wind direction in tropical cyclones using C-band dual-polarization synthetic aperture radar," *IEEE Trans. Geosci. Remote Sens.*, vol. 58, no. 2, pp. 1450–1462, Feb. 2019.
[25] M. Portabella, A. Stoffelen, and J. A. Johannessen, "Toward an optimal inversion method for synthetic aperture radar wind retrieval," *J. Geophys. Res., Oceans*, vol. 107, no. C8, pp. 1–1, 2002.
[26] A. A. Mouche, B. Chapron, B. Zhang, and R. Husson, "Combined co-and cross-polarized sar measurements under extreme wind conditions," *IEEE Trans. Geosci. Remote Sens.*, vol. 55, no. 12, pp. 6746–6755, Dec. 2017.
[27] G. Levy and R. Brown, "Detecting planetary boundary layer rolls from SAR," *Remote Sens. Pacific Ocean Satell.*, vol. 128, 1998, Art. no. 134.
[28] Y. Zhao, X.-M. Li, and J. Sha, "Sea surface wind streaks in spaceborne synthetic aperture radar imagery," *J. Geophys. Res.: Oceans*, vol. 121, no. 9, pp. 6731–6741, 2016.
[29] G. Levy, "Boundary layer roll statistics from SAR," *Geophys. Res. Lett.*, vol. 28, no. 10, pp. 1993–1995, 2001.
[30] J. E. Stopa, F. Ardhuin, B. Chapron, and F. Collard, "Estimating wave orbital velocity through the azimuth cutoff from space-borne satellites," *J. Geophys. Res., Oceans*, vol. 120, no. 11, pp. 7616–7634, 2015.
[31] Z. Jiang and W. Zhang, "The evaluation of damped newton variational ocean wind retrieval method," *Adv. Space Res.*, vol. 67, no. 6, pp. 1887–1895, 2021.
[32] N. Dalal and B. Triggs, "Histograms of oriented gradients for human detection," in *Proc. IEEE Comput. Soc. Conf. Comput. Vis. Pattern Recognit.*, 2005, vol. 1, pp. 886–893.
[33] CSA, "RadarSat-2," [Online]. Available: https://www.asc-csa.gc.ca/eng/satellites/radarsat2/what-is-radarsat2.asp/
[34] G.-J. Van Zadelhoff, A. Stoffelen, P. Vachon, J. Wolfe, J. Horstmann, and M. Belmonte Rivas, "Retrieving hurricane wind speeds using cross-polarization c-band measurements," *Atmospheric Meas. Techn.*, vol. 7, no. 2, pp. 437–449, 2014.
[35] B. Zhang, W. Perrie, J. A. Zhang, E. W. Uhlhorn, and Y. He, "High-resolution hurricane vector winds from C-band dual-polarization SAR observations," *J. Atmospheric Ocean. Technol.*, vol. 31, no. 2, pp. 272–286, 2014.
[36] G. Zhang, W. Perrie, X. Li, and J. A. Zhang, "A hurricane morphology and sea surface wind vector estimation model based on C-band cross-polarization SAR imagery," *IEEE Trans. Geosci. Remote Sens.*, vol. 55, no. 3, pp. 1743–1751, Mar. 2017.
[37] B. Zhang, A. A. Mouche, and W. Perrie, "First quasi-synchronous hurricane quad-polarization observations by C-band radar constellation mission and RADARSAT-2," *IEEE Trans. Geosci. Remote Sens.*, vol. 60, pp. 1–10, Mar. 2022.
[38] ESA, "Sentinel-1," [Online]. Available: https://www.esa.int/Applications/Observing_the_Earth/Copernicus/Sentinel-1/Introducing_Sentinel-1/
[39] J. A. Knaff et al., "Estimating tropical cyclone surface winds: Current status, emerging technologies, historical evolution, and a look to the future," *Trop. Cyclone Res. Rev.*, vol. 10, no. 3, pp. 125–150, 2021.
[40] IFREMER, "SHOC - satellite hurricane observation campaign," [Online]. Available: https://cerweb.ifremer.fr/amouche/shoc/shoc.html
[41] K.-H. Chou, C.-C. Wu, P.-H. Lin, and S. Majumdar, "Validation of QuikSCAT wind vectors by dropwindsonde data from dropwindsonde observations for typhoon surveillance near the Taiwan region (DOTSTAR)," *J. Geophys. Res., Atmos.*, vol. 115, no. D2, pp. 1–11, 2010.
[42] K.-H. Chou, C.-C. Wu, and S.-Z. Lin, "Assessment of the ascat wind error characteristics by global dropwindsonde observations," *J. Geophys. Res., Atmos.*, vol. 118, no. 16, pp. 9011–9021, 2013.
[43] J. L. Franklin, M. L. Black, and K. Valde, "GPS dropwindsonde wind profiles in hurricanes and their operational implications," *Weather Forecasting*, vol. 18, no. 1, pp. 32–44, 2003.
[44] *ASCAT Wind Product User Manual*, EUMETSAT OSI SAF, KNMI, De Bilt, Netherlands, 2019, Version 1.16. [Online]. Available: https://scatterometer.knmi.nl/
[45] J. Vogelzang, A. Stoffelen, A. Verhoef, J. De Vries, and H. Bonekamp, "Validation of two-dimensional variational ambiguity removal on seawinds scatterometer data," *J. Atmospheric Ocean. Technol.*, vol. 26, no. 7, pp. 1229–1245, 2009.
[46] A. Stoffelen et al., "C-band high and extreme-force speeds (CHEFS)-Final report," 2020. [Online]. Available: www.eumetsat.int/CHEFS
[47] S. Rémy et al., "Description and evaluation of the tropospheric aerosol scheme in the European centre for medium-range weather forecasts (ECMWF) integrated forecasting system (IFS-AER, cycle 45R1)," *Geosci. Model Develop.*, vol. 12, no. 11, pp. 4627–4659, 2019.
[48] J. A. Zhang and E. W. Uhlhorn, "Hurricane sea surface inflow angle and an observation-based parametric model," *Monthly Weather Rev.*, vol. 140, no. 11, pp. 3587–3605, 2012.
[49] W. Ni, A. Stoffelen, and K. Ren, "Hurricane eye morphology extraction from sar images by texture analysis," *Front. Earth Sci.*, vol. 16, no. 1, pp. 190–205, 2022.
[50] K. R. Knapp, M. C. Kruk, D. H. Levinson, H. J. Diamond, and C. J. Neumann, "The international best track archive for climate stewardship (IBTrACS) unifying tropical cyclone data," *Bull. Amer. Meteorological Soc.*, vol. 91, no. 3, pp. 363–376, 2010.
[51] K. R. Knapp, H. J. Diamond, J. P. Kossin, M. C. Kruk, and C. J. Schreck, "International best track archive for climate stewardship (IBTrACS) project, version 4," *NOAA Nat. Centers Environ. Inf.*, 2018.
[52] W. Ni, A. Stoffelen, K. Ren, and X. Yang, "Tropical cyclone intensity estimation from spaceborne microwave scatterometry and parametric wind models," *IEEE J. Sel. Topics Appl. Earth Observ. Remote Sens.*, vol. 15, pp. 4719–4729, Jun. 2022.
[53] X. Li, W. Zheng, X. Yang, Z. Li, and W. G. Pichel, "Sea surface imprints of coastal mountain LEE waves imaged by synthetic aperture radar," *J. Geophys. Res., Ocean.*, vol. 116, no. C2, pp. 1–10, 2011.
[54] X. Li, W. Zheng, X. Yang, J. A. Zhang, W. G. Pichel, and Z. Li, "Coexistence of atmospheric gravity waves and boundary layer rolls observed by SAR," *J. Atmospheric Sci.*, vol. 70, no. 11, pp. 3448–3459, 2013.
[55] R. Husson et al., "Wind direction estimation and accuracy retrieval from sentinel-1 sar images under thermal and dynamical unstable conditions," in *Proc. IEEE Int. Geosci. Remote Sens. Symp.*, 2021, pp. 7588–7591.
[56] F. Fetterer, D. Gineris, and C. C. Wackerman, "Validating a scatterometer wind algorithm for ERS-1 SAR," *IEEE Trans. Geosci. Remote Sens.*, vol. 36, no. 2, pp. 479–492, Mar. 1998.
[57] G. K. Carvajal, L. E. Eriksson, and L. M. Ulander, "Retrieval and quality assessment of wind velocity vectors on the ocean with C-band SAR," *IEEE Trans. Geosci. Remote Sens.*, vol. 52, no. 5, pp. 2519–2537, May 2014.

Weicheng Ni (Student Member, IEEE) received the B.S. degree in geophysical information science from Zhejiang University, Hangzhou, China, in 2017. He is currently working toward the Ph.D. degree in computer science and technology with the National University of Defense Technology, Changsha, China.

He is currently a Visiting Scholar with the Royal Netherlands Meteorological Institute, De Bilt, The Netherlands, and is working on the intercalibration between scatterometer data and synthetic aperture radar data.

Ad Stoffelen (Fellow, IEEE) received the M.Sc. degree in physics from the Technical University of Eindhoven, Eindhoven, The Netherlands, in 1987, and the Ph.D. degree in meteorology on scatterometry from the University of Utrecht, Utrecht, The Netherlands, in 1998.

He currently leads a group on active satellite sensing with the Royal Netherlands Meteorological Institute, De Bilt, The Netherlands, and is involved in topics from future missions and retrieval to 24/7 operations, user training, and services. He is also deeply involved in the European Space Agency ADM-Aeolus Doppler Wind Lidar mission.

Kaijun Ren (Member, IEEE) received the B.S. degree in applied mathematics and the M.S. and Ph.D. degrees in computer science from the National University of Defense Technology, Changsha, China, in 1998, 2003, and 2008, respectively.

He is currently a Professor with the College of Meteorology and Oceanography and the College of Computer, National University of Defense Technology. His current research interests include high-performance computing, cloud computing, Big Data, and their interdisciplinary applications in ocean science and meteorology areas.